New Journal of Physics
The open access journal at the forefront of physics

Deutsche Physikalische Gesellschaft DPG IOP Institute of Physics

PAPER

Nanoscale mechanical surface properties of single crystalline martensitic Ni–Mn–Ga ferromagnetic shape memory alloys

To cite this article: A M Jakob *et al* 2012 *New J. Phys.* **14** 033029

View the article online for updates and enhancements.

Related content

- Nanoscale magneto-structural coupling in as-deposited and freestanding single-crystalline Fe_7Pd_3 ferromagnetic shape memory alloy thin films
- Structural defects in Fe–Pd-based ferromagnetic shape memory alloys: tuning transformation properties by ion irradiation and severe plastic deformation
- Mechanical properties and twin boundary drag in Fe–Pd ferromagnetic shape memory foils—experiments and *ab initio* modeling

Recent citations

- Elastic constants determination of anisotropic materials by depth-sensing indentation
Caterina Lamuta
- Localized deformation in Ni-Mn-Ga single crystals
Paul H. Davis *et al*
- Crystallography of Martensitic Transformation in Epitaxial Ni50 Mn30 Ga20 Thin Film
Bo Yang *et al*

This content was downloaded from IP address 194.95.157.48 on 29/09/2020 at 08:20

New Journal of Physics
The open-access journal for physics

Nanoscale mechanical surface properties of single crystalline martensitic Ni–Mn–Ga ferromagnetic shape memory alloys

A M Jakob[1,2], **M Müller**[1,2], **B Rauschenbach**[1,3] **and S G Mayr**[1,2,3,4]

[1] Leibniz-Institut für Oberflächenmodifizierung (IOM), Permoserstr. 15, 04318 Leipzig, Germany

[2] Translationszentrum für regenerative Medizin (TRM), Universität Leipzig, Germany

[3] Fakultät für Physik und Geowissenschaften, Universität Leipzig, Germany

E-mail: alexander.jakob@iom-leipzig.de and stefan.mayr@iom-leipzig.de

New Journal of Physics **14** (2012) 033029 (16pp)
Received 18 January 2012
Published 16 March 2012
Online at http://www.njp.org/
doi:10.1088/1367-2630/14/3/033029

Abstract. Located beyond the resolution limit of nanoindentation, contact resonance atomic force microscopy (CR-AFM) is employed for nano-mechanical surface characterization of single crystalline 14M modulated martensitic Ni–Mn–Ga (NMG) thin films grown by magnetron sputter deposition on (001) MgO substrates. Comparing experimental indentation moduli—obtained with CR-AFM—with theoretical predictions based on density functional theory (DFT) indicates the central role of pseudo plasticity and inter-martensitic phase transitions. Spatially highly resolved mechanical imaging enables the visualization of twin boundaries and allows for the assessment of their impact on mechanical behavior at the nanoscale. The CR-AFM technique is also briefly reviewed. Its advantages and drawbacks are carefully addressed.

[4] Author to whom any correspondence should be addressed.

© IOP Publishing Ltd and Deutsche Physikalische Gesellschaft

Contents

1. Introduction

Yielding magnetically switchable strains of up to 10% in the 14M modulated martensitic phase by magnetically induced reorientation of variants, Ni–Mn–Ga (NMG)-based ferromagnetic shape memory alloys (FSMA) have attracted much interest since their discovery towards the end of the last millennium [1–3]. While active bulk single crystals are well established—and even commercially available within actuators—at this point [5], miniaturization as functional thin films remains an unresolved challenge. Prerequisites for technically meaningful films with maximum attainable strains are (i) a 14M modulated martensitic phase at room temperature, (ii) single crystallinity, (iii) highly mobile twin boundaries and (iv) the absence of external (i.e. substrate) constraints. It was demonstrated recently that epitaxy on an MgO (001) substrate from a magnetron sputtering source can successfully be employed to cope with challenges (i) and (ii) [4], whereas freestanding films can readily be obtained by subsequent lift-off approaches [5, 6] (as a remedy for (iv)). However, the understanding of deformation mechanics during reorientation of martensite variants as well as austenite–martensite transition (AMT) in the presence of open surfaces or reduced dimensionality is far from complete. While it is basically well established that the motion of twin boundaries (TBs) mediates the macroscopics of AMT (see, e.g., [7] and reference therein for a review on macroscopics), a quantitative experimental characterization from a nanomechanical point of view is still lacking. Since it might be tempting to consider nanoindentation as the technique of choice within this scope, there is a need to stress that with tip radii and indentation depths of the order of a tenth of a micron, resolution clearly proves to be insufficient. Inspired by early suggestions [8, 9], the capability of CR-AFM to assess mechanical response at the nanoscale on FSM materials was explored and demonstrated to be perfectly suitable to quantify nanomechanical properties at surfaces [10] in the present work.

[5] AdaptaMat Ltd, Helsinki, Finland.

2. Theoretical aspects

2.1. 14*M modulated martensitic Ni–Mn–Ga*

2.1.1. Crystal structure. Based on cross-sectional high-resolution transmission electron microscopy (HRTEM) investigations and x-ray diffraction [4], it was already shown that sputter deposited single-crystalline NMG films on MgO (001) substrates reside in an orthorhombic 14M modulated martensitic phase with lattice parameters $a = 0.612$, $b = 0.578$ and $c = 0.554$ nm at room temperature (see section 3 for sample preparation details). The surface morphology is characterized by micro-scale domains with a regular twin variant pattern (see figure 1(a)). A representative lamella cut along a (110) plane of the MgO substrate (or equivalently the (010) plane of austenitic NMG) is exemplarily shown in figure 1(c). As summarized in figure 1(d), twinning generally can occur on {110} planes, while only one of the latter is observed within each domain. Residing in a 45° angle with two of the {100} planes and being normal to the other, the intradomain stripe pattern under 45° to the surface (as shown in the cross-sectional TEM image in figure 1(c)) is readily understood. Morphology on the surface (figure 1(b)) thus reflects a cross section of the twin variant structure. The intravariant structure, on the other hand, was always determined to be 14M martensite in HRTEM, while the *b*-axis of the orthorhombic cell proved to be directed in plane with the surface and twinning planes—as sketched in figure 1(b). Also shown is the orientation of the TB (red line). Within the present context it is important to emphasize that, on both sides of a surface stripe, an asymmetry in material properties can thus arise (i) for crystallographic reasons (orientation of the *a*- or *c*-axis normal to the surface) and (ii) because of the inclination of the TB with respect to both variants.

2.1.2. Density functional theory (DFT) predictions of elastic properties. DFT [11] based on total energy calculations is performed to predict mechanical properties of the 14M modulated Ni_2MnGa martensite phase. Electronic structure calculations employed ultrasoft pseudopotentials [12–14] with nonlinear core corrections [15] based on the atomic reference configurations [Ar] $3d^9 4s^1$, [Ar] $3d^5 4s^2$ and [Ar] $3d^1 04s^2 4p^1$ for Ni, Mn and Ga, respectively[6], and a plane-wave basis set, as implemented in the `pwscf` code [16]. The effects of exchange and correlation are treated according to the Perdew–Burke–Ernzerhof functional [17] with spin-polarized generalized gradient correction. Brillouin zone integration (using $10 \times 8 \times 4$ up to $20 \times 16 \times 8$ Monkhorst–Pack grids [18]) using the Methfessel–Paxton smearing [19] (0.27 eV), as well as the energy cut-off of the plane-wave basis set (612 eV) and augmentation charges (6123 eV) were optimized to obtain energy and stress convergence better than 0.5 meV atom^{-1} and 2%, respectively, after structural relaxation runs. Taking the unit cell of the 14M modulated Ni_2MnGa martensite phase proposed by Zayak *et al* [20] as the starting point, the present DFT study first relaxed the lattice vectors and basis towards equilibrium for the currently employed conditions. As the resulting reference cell agrees to within less than 1% with the suggestion of Zayak *et al* [20], this corroborates the accuracy of both treatments—in particular because they can be considered to be methodologically independent. Within the present study, ionic and cell relaxations are always realized with the Broyden–Fletcher–Goldfarb–Shanno (BFGS) scheme as implemented in `pwscf`. For the sake of comparison with experiments, it is desirable to determine the tensor of elasticity C_{ij} (given in the Voigt notation in the following) within the

[6] Files `Ni.pbe-nd-rrkjus.UPF`, `Mn.pbe-sp-van.UPF` and `Ga.pbe-n-van.UPF`, available at http://www.pwscf.org

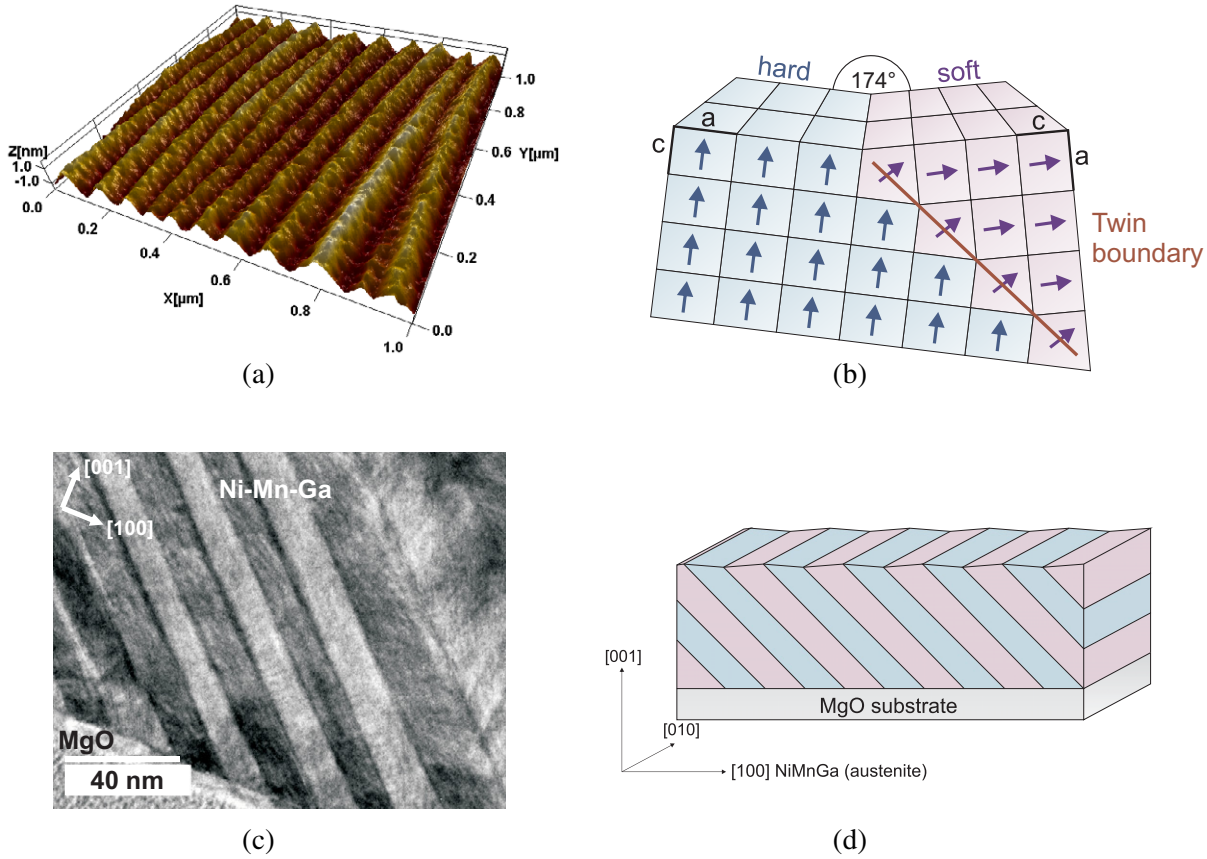

Figure 1. (a) AFM topography reflects a martensitic surface relief, crystallographically originating from neighboring variants with different orientations of the orthorhombic unit cell to the surface normal. (b) Corresponding schematic: with $c/a \approx 0.905$ in 14M martensite, neighboring variants are inclined by an angle of about 6°. The small arrows indicate the easy axis of magnetization. (c) Cross-sectional transmission electron microscopy measurement of a single crystalline 14 M modulated NMG thin film (400 nm thickness) epitaxial grown on MgO (001). (d) Related schematic: within {010} TEM cross-sections, {101} twinning planes appear under 45° to the surface. Generally, twinning planes are always found to be of the {101} type, while pure 14M martensite prevails within the variants.

orthonormal coordinate system given by the lattice vectors [100], [010] and [001] of the parental austenitic phase. It is worth emphasizing within this context that while these vectors reflect the probing directions in the present experiments, they do not exactly reflect the strictly monoclinic nature of 14M modulated martensite (although deviations with $\leqslant 4^\circ$ in the calculations are only minor). Determination of C_{ij} in the present DFT calculations is performed 'manually' by straining the unit cell by ± 0.5 and $\pm 1\%$ in the directions of interest, while determinating the resulting stress response after allowing for ionic relaxation in DFT calculations and finally performing linear regression for determination of the corresponding C_{ij} (equation (1)). As a double check, the tensor of elasticity was also calculated from the ground-state energy as a function of strain, which after fitting to the Murnaghan equation of state yielded identical results

within the error bars. However, the experimental approach based on the CR-AFM technique yields an indentation modulus M, since a cantilever tip is applied on the sample surface. The resulting elastic response is thus determined by an interplay of elastic constants given in C_{ij} and additionally depends on the tip shape as well as indentation direction. The theory behind calculating the M of mechanically anisotropic solids is challenging but has been revealed and discussed intensively ([21, 22] and references therein).

$$C_{ij} = \begin{pmatrix} 206 & 160 & 141 & 0 & 0 & 0 \\ 160 & 230 & 101 & 0 & 0 & 0 \\ 141 & 101 & 253 & 0 & 0 & 0 \\ 0 & 0 & 0 & 84 & 0 & 0 \\ 0 & 0 & 0 & 0 & 102 & 0 \\ 0 & 0 & 0 & 0 & 0 & 112 \end{pmatrix} \text{GPa}. \tag{1}$$

Based on the work of Vlassak *et al* [21], M was calculated numerically from C_{ij} for different indentation directions, assuming a spherical tip shape. The results are listed in table 2 and will be consulted for a comparison with experimental data (see section 4).

2.2. The contact resonance atomic force microscopy (CR-AFM) technique

CR-AFM is a dynamic mechanical spectroscopy method, utilizing cantilever eigenfrequencies during material contact to get information about mechanical surface properties. Therefore, a cantilever is applied to the sample surface with a defined static load F_{L} (figure 2(a)). Additionally, an ultrasound transducer feeds wide band longitudinal acoustic waves into the sample and thus excites the cantilever to vibrate. In order to get a correlation between the cantilever's contact resonance frequency (CRF) and the sample's indentation modulus, a model of beam bending dynamics needs to be connected to a contact mechanics theory. The fundamentals are briefly reviewed here. A deeper insight into this topic can be found in [23, 24].

2.2.1. Beam bending model. An AFM cantilever possesses a set of individual eigenfrequencies $f_{i,\mathrm{res}} (i \in \mathbb{N})$, which are determined by a bending model based on the beam bending differential equation and proper boundary conditions. Flexural undamped modes of a beam with length l, cross sectional area $A = b\,d$ and mass density ρ are given by

$$\frac{\partial^2}{\partial x^2}\left(E\,I\,\frac{\partial^2 u(x,t)}{\partial x^2}\right) + \rho A \frac{\partial^2 u(x,t)}{\partial t^2} = 0 \qquad \begin{matrix} \frac{\partial^n u(x)}{\partial x^n}\big|_{x=0} = 0, \ n = 0, 1, \\ \frac{\partial^n u(x)}{\partial x^n}\big|_{x=l} = 0, \ n = 2, 3, \end{matrix} \tag{2}$$

where E is the elastic modulus and I describes the area moment of inertia, which is calculated by $b\,d^3/12$ for an ideal rectangular-shaped beam. The boundary conditions $n = 0, 1, 2, 3$ ensure a one-sided clamping of the beam at $x = 0$. For small vibration amplitudes around the cantilever's static equilibrium deflection, the repulsive tip–surface interaction can be described by a linear force approach according to $F = -ku(x)|_{x=l}$, with 'contact stiffness' k. Compared to a free cantilever, boundary conditions $n = 2, 3$ are modified and resonance frequencies $f_{i,\mathrm{res}}$ will shift in the presence of $k \neq 0$. Equation (2) has been studied intensively and the f versus k dependence is discussed considering a wide range of influences such as the tilt angle of cantilever, tip height, lateral forces, etc. However, equation (2) cannot be solved analytically for non-ideal rectangular-shaped beams consisting of elastic anisotrope materials, which is

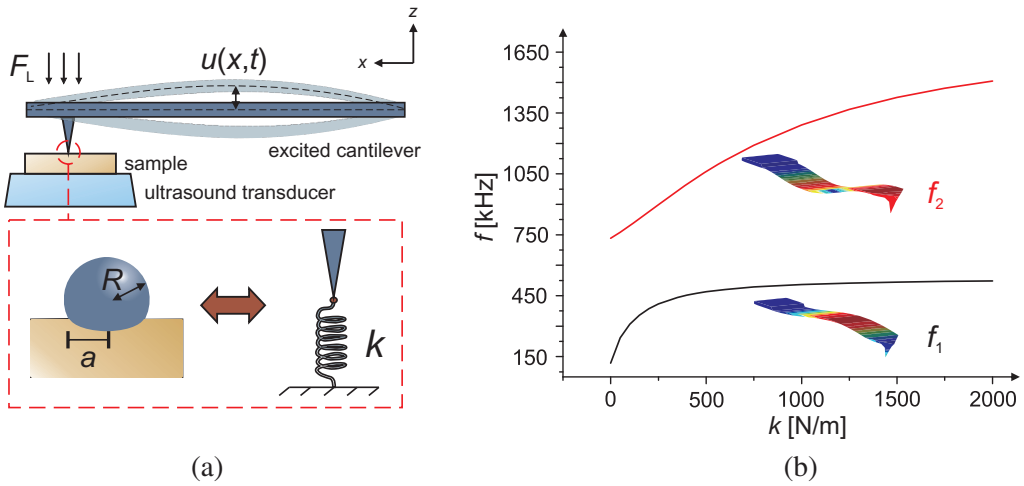

Figure 2. (a) Principle of CR-AFM analysis: longitudinal acoustic waves, emitted by an ultrasound transducer beneath the sample, excite a loaded cantilever to resonant vibration. Tip–surface contact is linearized with a spring constant k. An appropriate contact mechanics model like the Hertzian theory associates k with the effective surface indentation modulus M. (b) FEM modelled dispersion relation of $f_{i,\mathrm{res}}$ versus k simulated for a spring-coupled Bruker MPP130 cantilever. Shown are solutions of the first two bending modes. A cantilever tilt-angle of 11° relative to the spring is considered. The inset graphics illustrate corresponding bending displacements $u(\vec{x}, t_0)$ of each mode for $k = 1000\,\mathrm{N\,m^{-1}}$.

typically the case for commercial AFM cantilevers. A powerful numerical approach consists in finite-element modelling (FEM) as already shown in [25]. Figure 2(b) illustrates the dispersion relation f versus k for the first two eigenmodes $f_{1,\mathrm{res}}$ and $f_{2,\mathrm{res}}$, calculated by FEM[7] of a Bruker MPP130 cantilever ($f_{1,\mathrm{free}} = 116\,\mathrm{kHz}$, $f_{2,\mathrm{free}} = 726\,\mathrm{kHz}$). Obviously, the dispersion curves can be separated in a region with nearly linear slope ($\mathrm{d}\,f_{i,\mathrm{res}}/\mathrm{d}\,k \neq 0$), resulting in high sensitivity to surface stiffness, as well as a region where the curve saturates (not suitable for CR-AFM imaging). It is also noticeable that sensitive regions shift to higher values for higher-order eigenmodes. Depending on influences such as tip dimensions, cantilever stiffness and surface rigidity, a proper eigenmode for optimum sensitivity needs to be selected.

2.2.2. Tip–surface contact model. The beam bending model was applied to link the cantilever–eigenmodes $f_{i,\mathrm{res}}$ to the contact stiffness k. In a second step, k is associated with the material-specific indentation modulus M. Based on the Hertzian contact theory for anisotropic materials [26] and according to Vlassak and Nix [27], one defines

$$k = \frac{\mathrm{d}\,F_\mathrm{L}}{\mathrm{d}\,u} = 2\,M\sqrt{\frac{A}{\pi}} = \begin{cases} \sqrt[3]{6\,F_\mathrm{L}\,R\,M^2}, & \text{spherical indenter,} \\ 2\,R\,M, & \text{flat punch,} \end{cases} \tag{3}$$

[7] FEM calculations used COMSOL Multiphysics 3.5a.

Table 1. Specifications of the sample NMG-1.

Composition (at.%)			Thickness (nm)	$\frac{e}{a}$	T_M (K)	T_A (K)	T_C (K)
Ni	Mn	Ga					
48 ± 1	31 ± 1	21 ± 0.5	400 ± 10	7.6 ± 0.05	303 ± 1	307 ± 1	363 ± 1

whereas A describes the tip–surface contact area and M includes indentation moduli of tip- and surface-material according to

$$\frac{1}{M} = \frac{1}{M_{\text{tip}}} + \frac{1}{M_{sample}}. \tag{4}$$

In the more general case of elastic anisotropic materials, the middle part of equation (3) still holds as long as a threefold or fourfold rotational symmetry, perpendicular to the surface plane, is ensured [27].

Finally, by combining equation (3) and the dispersion relation of the bending model (figure 2(b)), a correlation between the experimentally observable CRF $f_{i,\text{res}}$ and the sample's indentation modulus M_{sample} is established. One should note that the tip radius R is just an equivalent of the tip-curvature rather than the lateral tip size, which means that even small tips (of several nm in size) might have high radii (e.g. a flat punch yields $R = \infty$).

3. Experiment

3.1. Sample preparation

As described in [4], almost perfect $Ni_{49}Mn_{32}Ga_{19}$ single crystals were grown on MgO (001) substrate[8] by magnetron sputter deposition from a multicompound target[9]. Prior to film deposition, the chamber was baked overnight to ensure a base pressure at least within the high-vacuum (HV) regime and to dehydrate the MgO substrate. After 300 s of presputtering, preparation of 400 nm thick films was performed at 600 °C substrate temperature and a deposition rate of 0.19 nm s^{-1}. The latter was realized by using an Ar pressure of 3×10^{-3} mbar and a nominal sputtering power of 50 W (dc). After deposition, samples were routinely checked for their chemical composition using energy dispersive x-ray spectroscopy (EDX), for crystal structure by means of x-ray diffraction analysis (XRD) and for surface topography by scanning electron microscopy (SEM). Furthermore, temperature-dependent electrical resistivity measurements were used to gain the martensite transition temperature T_M and the Curie-temperature T_C (table 1) [28].

3.2. The CR-AFM setup

The current setup is based on a programmable Asylum Research MFP-3D SA AFM[10], which is additionally equipped with an ultrasound transducer directly underneath the sample.

[8] CrysTec GmbH, CrysTec Kristalltechnologie GmbH, Berlin, Deutschland.
[9] ACI Alloys, Inc., San Jose, CA, USA.
[10] Asylum Research, Santa Barbara, CA, USA.

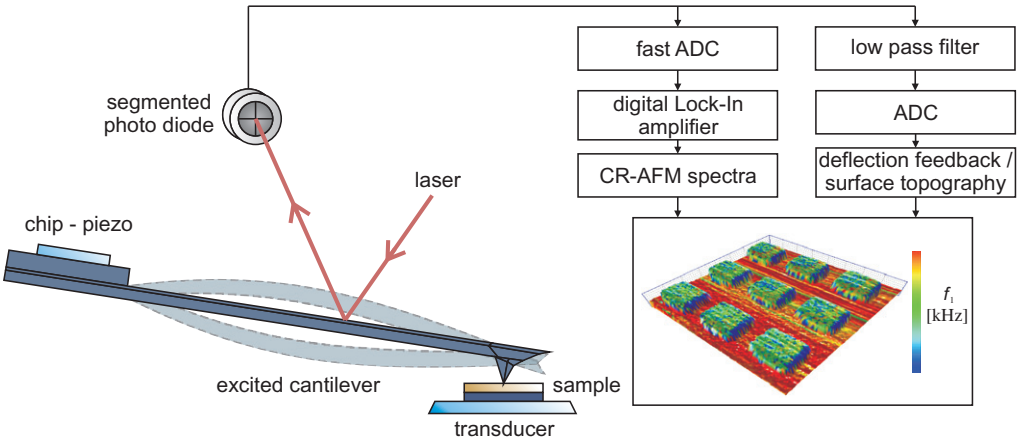

Figure 3. Scheme of the experimental CR-AFM setup. Cantilever excitation can be achieved by either a sample transducer or the cantilever shaking piezo. A segmented photodiode is sensitive to angular changes of the reflected laser spot caused by cantilever displacements. The digitized signal is split, filtered and post-processed in order to gain CRF $f_{i,\mathrm{res}}$ as well as topographic information. An exemplary CR-AFM image shows rectangular Ti patterns ($t \approx 100$ nm) on the Si substrate. The overlaid $f_{1,\mathrm{res}}$ colormap clearly reveals differing elastic properties of both domains.

As indicated in figure 3, the cantilever deflection is read out optically, whereby a laser spot is reflected from the cantilever's back side and detected by a photodiode. Finally, the AFM's 5 MHz ADC digitizes the signal. The low-frequency signal parts yield information about surface topography, whereas the high-frequency part contains contact resonance spectra. Two fast digital lock-in amplifiers, integrated in the AFM's field programmable gate array (FPGA), allow the identification of CRFs out of the high-frequency spectra. The whole acquisition process is carried out dynamically at each point (pixel) during an image scan. Besides this continuous *image-scan* mode, where the cantilever is kept engaged to the surface, the setup also allows *point-map* acquisition. In this mode, the tip only touches the surface at discrete points within a predefined $m \times n$ array to acquire $f_{i,\mathrm{res}}$. Since there is no lateral movement during contact, tip wear is low compared to *image-scanning*. This advantage is at the expense of significantly increased measuring duration due to continual engage–withdraw processes. It is preferable to use the *point-map* method if absolute quantitative information about the elastic surface modulus is of more interest than knowledge of spatially resolved elastic variations. Two Bruker MPP130 cantilevers (denoted as MPP130-1 and MPP130-2) were used for the measurements discussed here. Effective stiffnesses of $k_{130-1} = 13\,\mathrm{N\,m^{-1}}$ and $k_{130-2} = 11.5\,\mathrm{N\,m^{-1}}$ were determined via FEM modelling and experimentally confirmed by the thermal noise method [29]. The first two free bending modes amount to $f_{1,130-1} = 121$ kHz, , $f_{2,130-1} = 755$ kHz and $f_{1,130-2} = 116$ kHz, , $f_{2,130-2} = 726$ kHz, respectively.

3.3. Data acquisition and analysis

Since CR-AFM is not a standard-less measuring method, quantitative determination of elastic surface properties call for proper reference samples with known indentation moduli. As is

usual in CR-AFM analysis, [001]-grown single-crystalline silicon ($M_{Si} = 165\,GPa$) and fused silica ($M_{FS} = 75\,GPa$) were utilized. In the following, a short overview about identifying the indentation modulus M_{sample} of an unknown sample is given. A procedure typically applied in the CR-AFM community [30] is therefore followed here.

The measuring series consists in acquiring a 6×4 *point-map* on every sample to gain the corresponding average second CRF $\langle f \rangle_{2,res}$. The scanned area extended to $1\,\mu m^2$ in size. Those measuring series were performed several times on different sample regions in order to avoid flawed data due to tip wear (change in tip radius R) and surface artifacts, respectively. This measuring process was repeated at two different applied loads F_L. For the sake of reproducibility, the whole procedure was carried out again utilizing a second MPP130 cantilever possessing a significantly more blunted tip. All measurements were realized at room temperature. Once $f_{2,res}$ is known for each sample, the contact stiffness k can be associated using the dispersion relation figure 2(b). The next step consists in calculating the effective tip indentation modulus M_{tip} by means of known M_{Si} and M_{FS}. For this purpose, one solves the ratio k_1/k_2 by substituting equation (4) into equation (3):

$$\frac{k_1}{k_2} = \left(\frac{M_1}{M_2}\right)^m, \quad m = \begin{cases} 2/3, & \text{spherical tip,} \\ 1, & \text{flat punch.} \end{cases} \tag{5}$$

Finally, equation (5) can be used again to calculate M_{sample}.

4. Results and discussion

4.1. Elastic properties: DFT versus CR-AFM

Following the analytical approach described in the previous section, the indentation modulus M_{NMG} was measured along the [001] direction of the sample NMG-1, which remained attached to the MgO substrate throughout the experiments. Force–distance measurements, previously acquired for the sample, revealed that adhesion forces can be neglected. Together with numerical data of DFT calculations, experimental results are listed in table 2. Indentation moduli M_{NMG} were calculated assuming a flat and a spherical tip, respectively—yielding very similar results. It can be seen that the absolute error of $\langle f \rangle_{2,res}$ (standard deviation σ) for NMG-14M is higher than that of the reference samples, which could have its origin in the characteristic surface structure (see figure 1(a)). This fact will be discussed in the next section. One more aspect is conspicuous—compared to DFT results, experimentally observed indentation moduli are significantly reduced. Conceivable explanations for this discrepancy can be given considering pseudoplasticity and elasticity due to inter-martensitic phase transformation characteristics in NMG, respectively.

As for pseudoplasticity, a schematic stress–strain diagram upon loading is sketched in figure 4(a): starting with single variant martensite, region I describes stress–strain dependence according to linear elasticity. Beyond a critical stress σ_c (viz the 'twinning stress') pseudoplastic deformation occurs while tetragonal unit cells successively reorient (TB motion). This process is marked as region II. Once all unit cells are reoriented, the material again shows a linear elastic behavior (region III) at moderate further deformations. The magnitude of σ_c for inducing TB motion substantially depends on parameters such as the straining direction and sample temperature, as well as intrinsic stress fields (e.g. lattice defects due to off-stoichiometry and other impurities). In the case of martensite NMG, it was shown that $\sigma_c \approx 2$–$200\,MPa$ is sufficient

Table 2. CR-AFM data and numerical DFT predictions of the indentation modulus M for NMG-1.

	Experimental results								
F_L (nN)	300	500	300	500	310	500		**DFT**	
	MPP130-1								
	$\langle f \rangle_{2,res}$ (kHz)		k (N m^{-1})		M (GPa)		$M_{[001]}$	$M_{[010]}$ (GPa)	$M_{[100]}$
Si	1218 ± 3	1237 ± 3	861 ± 6	909 ± 6	165[a]				
FS	1170 ± 3	1191 ± 3	750 ± 6	798 ± 6	75[a]				
NMG-1	1150 ± 7	1178 ± 7	706 ± 15	768 ± 15	**59 ± 6**	**63 ± 6**	**215**	**193**	**175**
	Experimental results								
F_L (nN)	310	470	310	470	310	470		**DFT**	
	MPP130-2								
	$\langle f \rangle_{2,res}$ (kHz)		k (N m^{-1})		M (GPa)		$M_{[001]}$	$M_{[010]}$ (GPa)	$M_{[100]}$
Si	1034 ± 3	1056 ± 3	415 ± 4	449 ± 4	165[a]				
FS	1012 ± 3	1023 ± 3	383 ± 4	400 ± 4	75[a]				
NMG-1	1002 ± 5	1015 ± 5	366 ± 7	388 ± 7	**56 ± 6**	**64 ± 6**	**215**	**193**	**175**

[a] Supposed as given [24].

to cause pseudoplastic behavior [31, 32]. It is necessary to emphasize that pseudoplasticity implies an irreversibility, viz a remaining strain or, deformation upon unloading.

Martynov and Kokorin [32] proposed that pseudoplastic deformation, induced by external stresses, can be accompanied by pseudoelasticity due to inter-martensitic phase transitions (10M→14M→non-modulated), whereas each martensite phase remains stable within a certain temperature interval. Conversely, at constant temperature, increasing shear stresses will favor phases/modulations with increasing tetragonality (i.e. non-modulated martensite), as described by the Clausius–Clapyron equation. The loading curve under these conditions follows a shape qualitatively akin to figure 4(a), while unloading is fully reversible with a hysteresis. Since visible plastic deformations—as observed in pseudoplasticity—are absent from the present CR-AFM measurements, this particularly favors the occurrence of inter-martensitic pseudoelasticity as the more probable mechanism. Due to the employed boundary conditions, very limited size of the simulation cell and rather moderate applied stresses in the calculation of the tensor of elasticity, twin boundary motion or phase transformation is intrinsically excluded in the present DFT calculations. In other words, the stress–strain relation assessed in DFT currently corresponds to the pure elastic region I (red line in figure 4(a)). As can be seen in table 2, applied loads in CR-AFM measurements are typically in the range of 300–500 nN. Assuming a circular tip–surface contact area, related contact radii on NMG samples are calculated as $\{a_{c,flat} = 21\text{–}24\,\text{nm},\ a_{c,\,sphere} = 15\text{–}17\,\text{nm}\}$ for MPP130-1 and $\{a_{c,flat} = 14\,\text{nm},\ a_{c,\,sphere} = 10\,\text{nm}\}$ for MPP130-2. Corresponding average loading pressures p_m are thus in the ranges of 210–570 MPa (MPP130-1) and 900–2000 MPa (MPP130-2) and consequently larger than σ_c.

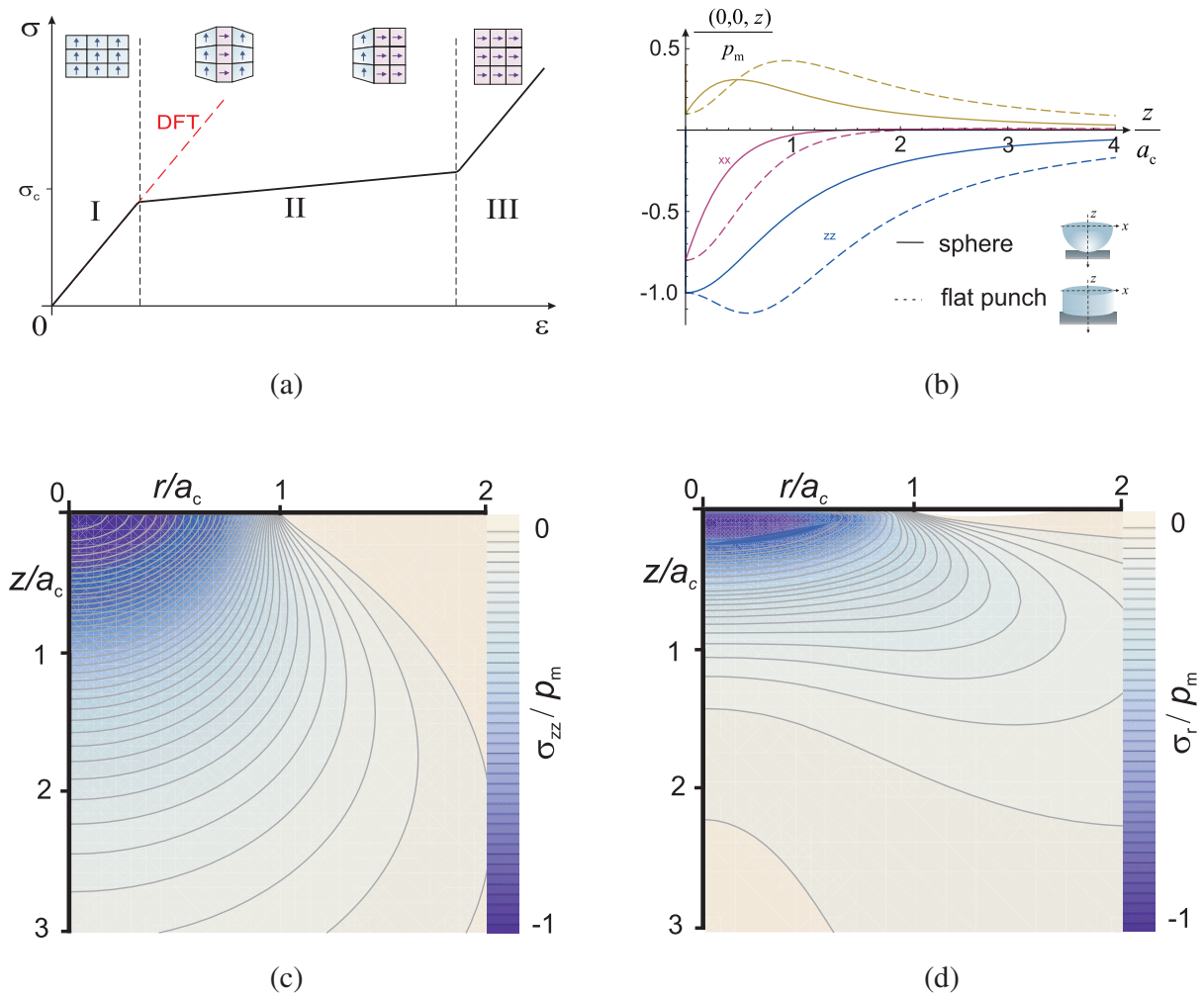

Figure 4. (a) Scheme of the loading curve in pseudo plastic and elastic materials. In both cases, the very low stress regime is characterized by elastic deformation (region I), typically followed by a plateau (region II) dominated by the 'resistivity' of twinning dislocation motion (leading to variant reorientation or inter-martensite phase transformation in the case of pseudo plasticity and elasticity, respectively). Upon completion of reorientation or transformation (regime III), elastic response is again observed. (b) Distributions of the uniaxial vertical stress σ_{zz}, uniaxial in-plane stress σ_{xx} and principal shear stress $\tau = |\sigma_{zz} - \sigma_{xx}|/2$ along the z-axis for a spherical and a flat indenter calculated according to Johnson [37]. A Poisson ratio of $\nu = 0.3$ was assumed. (c, d) Contour plots of the uniaxial vertical stress σ_{zz} and the radial stress σ_r, respectively, for a spherical tip ($\nu = 0.3$).

Nevertheless, the stress distribution in solids induced by indenters is complex and needs to be considered. Figures 4(c)–(d) show uniaxial stress distributions σ_{zz} ($\parallel$ to $\langle 001 \rangle$) and (σ_r) ($\perp$ to the surface plane), induced by a spherical indenter (normalized to p_m, the polar coordinates in surface plane). Referring to these stress distributions, the question arises as to whether

they can conform to the assumption of stress-induced pseudoplastic deformation and inter-martensitic transition. From a quantitative point of view, σ_{zz} and σ_r are large enough near the central region of the indentation spot to overcome σ_c. Moreover, shear forces arising due to lateral and depth gradients of both stress states can cause plane shuffling and consequently transitions between different martensitic phases. Existing shear stresses within the material additionally need to be taken into account, as they might interfere with the nano indentation process. A generalized Clausius–Clapeyron approach can describe a shift of the martensite transition temperature T_M due to thermal stresses within a film ($d\sigma_c/dT_M = 2.2\,\mathrm{MPa\,K^{-1}}$ [33–35]). Sources of shear stresses include (i) thermal stresses by differences in thermal expansions of film and substrate, (ii) epitaxy misfit stresses and (iii) lattice defects. With the known chemical composition and T_M (table 1) of NMG-1 as well as the phase diagram given in [36] and thermal expansion coefficients of film and MgO substrate, one can calculate the in-plane biaxial thermal tensile stress as $\sigma_{Th} = 10$–$110\,\mathrm{MPa}$. This rough estimation is due to the uncertainty of chemical composition in NMG-1 obtained by EDX measurements (see table 1). The orientation of σ_{Th}, however, results in a constructive superposition with σ_r since both are characterized by in-plane tensile straining the sample surface. Thermal stresses should thus not hinder possible pseudoplasticity as well as inter-martensitic transition provoked by the loaded cantilever tip. However, it was not possible for us to give a comparable quantitative estimation of stresses corresponding to (ii) and (iii) since the influence of substrate and related fixation of TB is poorly understood. Referring to the presence of different twin variants—with twin boundaries in between—the question arises how twin variants in figure 1(b) (variant 1: long a-axis out of the surface plane, variant 2: short c-axis out of the surface plane) differ in their mechanical properties. As will be shown in the next section, no recognizable differences between both crystal orientations were measured with CR-AFM. This finding clearly cannot be explained by a sole elastic response, since DFT predicts significantly different values for $M_{[100]}$ and $M_{[001]}$. As an additional confirmation of this picture, temperature-dependent CR-AFM measurements are currently carried out on as-deposited and lift-off films.

4.2. CR-AFM imaging: surface artifacts and twin boundaries

Since tip–surface contact at the nanoscale is a complex phenomenon influenced by various interaction mechanisms, AFM-based imaging techniques[11] often need to deal with disturbed data which complicate subsequent analysis. Regarding CR-AFM measurements presented here, surface roughness in particular strongly affects the contact area—resulting in CRF shifts that do not correspond to real mechanical characteristics. This key problem requires an even more critical review when surface features are of a similar lateral size to the scanning probe tip. The increased error of indentation modulus for NMG-1, mentioned in the previous section, can be assigned to that interplay, as illustrated in figure 5. The overlaid CRF colormap suggests asymmetric elastic properties of twin patterns. Considering schematic 1(b), one first tends to conclude that this behavior could be addressed to different orientations of orthorhombic unit cells (interchange of the a and c axes) on both sides of the pattern. This argument can be checked by rotating the whole sample around 180° and repeating the measurement. Pure mechanical influences would also cause a rotation of the CRF colormap. The experiment, however, does not confirm this initial guess (see figure 5), indicating artifacts due to topography and non-axis symmetric tip shape. This is confirmed by measurements with a more blunted tip and

[11] For example, magnetic force microscopy (MFM) and piezo force microscopy (PFM).

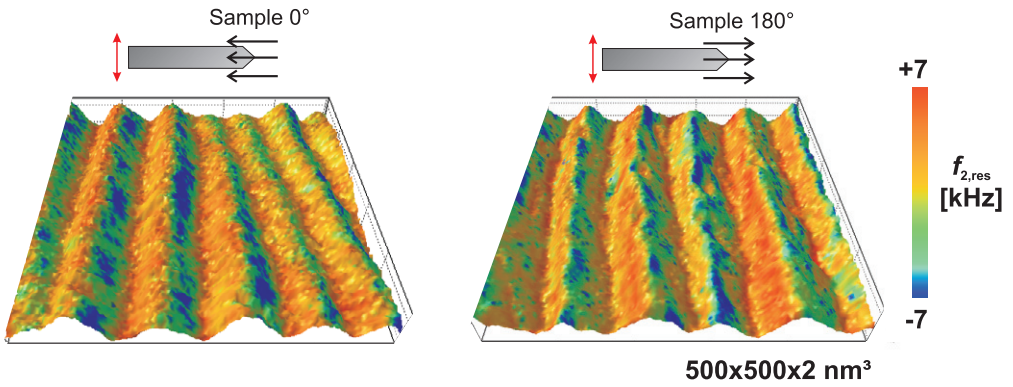

Figure 5. Exemplary topography map of NMG-1 and overlaid CR-AFM colormap measured with MPP130-1 at $F_L = 300\,\text{nN}$. Rotating the sample at 180° does not change CR-AFM information (not exactly the same measuring position). Pair-wise measurements at 0° and 180° sample orientation were repeated at four arbitrarily chosen positions and different scanning directions—yielding the same results like representative CR-AFM images for the utilized tip. Frequency shifts are caused by variations of contact area due to the interference of angular surface variations and asymmetric tip shape.

a shape closer to rotational symmetry. The CRF color-contrast for that tip is symmetrically distributed over the twin pattern, whereas elevated regions appear 'softer' than lower ones (not shown here) because of varying interaction area. However, a precise decomposition of CR-AFM contrast in real mechanical fluctuations, on the one hand, and surface artifacts, on the other hand, is non-trivial. Consequently, an elimination of twin structure surface features by changing the lattice orientation is helpful. One further NiMnGa sample (NMG-2) was produced with modified processing parameters. A lateral temperature gradient within the substrate was sustained during deposition. The chemical composition of NMG-2 is nearly identical to that of NMG-1. Besides the typical twin pattern (according to figure 1(a)) the sample additionally yields microscopic domains with a flat non-patterned surface ($\Delta\, h_{RMS} \approx 0.3\,\text{nm}$). A CR-AFM image utilizing a cantilever MPP130-1 was performed near the boundary of two domains (see figure 6). As can be seen, the non-patterned region clearly reveals a periodic mechanical contrast ('stripes') not corresponding to surface features. The in-plane angle of these stripes compared to the patterned twin domain amounts to exactly 45°. This can be understood considering constraints of epitaxial growth on MgO and figure 6. Non-patterned regions are characterized by a change of crystallographic orientation, where the *a*- and *c*-axis now lie in the surface plane (*b*-axis out of plane). Pure mechanical variations are thus only caused by highly ordered TB and amount to $\Delta M \approx \pm 4$ GPa, which is about one third lower than the error of M for NMG-1 (see table 2). From this comparison it can be seen that even slight surface features such as periodic twin structure can disturb CR-AFM data. One should remember that no surface damage is caused by CR-AFM imaging, as can be seen by comparing figures 5 and 1(a). It is also noticeable that these TB are highly ordered plane-like (viz two-dimensional) defects with an orientation perpendicular to the sample surface (see scheme (b) in figure 6) but drop M roughly about 8 GPa in total. Considering that the indentation modulus M is an average value over the tip–surface contact area of $A = \pi\, a_{c,\text{sphere}}^2$ with $a_{c,\text{sphere}} \geqslant 15\,\text{nm}$, one can conclude that

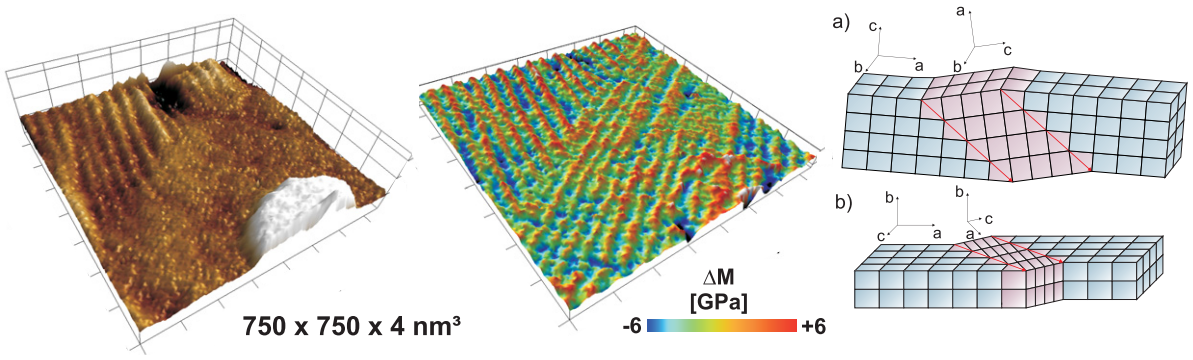

Figure 6. Left: AFM image at the boundary of two different domains of sample NMG-2. Center: the CR-AFM map reveals periodic variations ('stripes') within the non-patterned region. Their relative angle with respect to the twin patterns is 45° and can be attributed to TB. Right: schematics of crystal orientations within the two different domains. Scheme (a) presents crystal orientation usually occurring (patterned domains), whereas (b) illustrates the orientation of non-patterned domains.

the presence of TB significantly affects local mechanical characteristics. This finding perfectly agrees with the generally accepted notion that macroscopic deformation by reorientation of martensite variants at existing TB (movement of TB) is preferred to generating new TB within a martensite variant.

5. Conclusions

Elastic properties—i.e. elastic constants C_{ij} and corresponding indentation moduli M_{DFT}—of 14M modulated martensite Ni–Mn–Ga were calculated for the first time by a DFT approach. Considering DFT calculations of [38] for austenite, 5M modulated and non-modulated martensite Ni–Mn–Ga, the present data set gives suitable predictions regarding elastic behavior of 14M modulated Ni–Mn–Ga. These results were compared to an experimental indentation modulus M_{exp} of epitaxial grown 14M modulated Ni–Mn–Ga thin films, obtained with CR-AFM—a recent promising technique for non-destructive investigation of mechanical surface properties with nanoscale resolution. It was found that M_{exp} is about three times lower than M_{DFT}. Based on the results published in [32] and a consideration of stress distributions induced by an indenting cantilever tip, it is assumed that pseudoplastic deformation as well as pseudo elastic inter-martensite phase transitions could explain these findings. Complementary studies to verify these suggestions will be undertaken in the future. In particular, temperature-dependent CR-AFM measurements and comparisons to lift-off Ni–Mn–Ga thin films need to be carried out. Furthermore, limitations of CR-AFM were carefully investigated within the present work. In particular, highly periodic topographic features with lateral dimensions comparable to tip radii disturb experimental results and call for attentive data analysis. It was shown for the first time that lateral highly resolved CR-AFM mechanical contrast imaging enables the visualization of twin boundaries due to their characteristic influence on nanomechanical material properties. M_{exp} decreases about 13% at such highly ordered lattice defects for the utilized tip.

Acknowledgments

The authors are indebted to G Mahnke and Professor Dr M Seibt (Universität Göttingen) for TEM measurements, Dr C Vree for initially stimulating the present work by setting up the group's first CR-AFM setup back in 2007 [10] and F Szillat (IOM/TRM Leipzig) for fruitful discussions. Resistivity measurements and subsequent analysis provided by F Schmidt and Professor Dr M Grundmann (Universität Leipzig) are also acknowledged. We thank Dr S Vinzelberg (Atomic Force F&E GmbH, Germany) for support concerning AFM programming. This work was funded in part by the German Federal Ministry of Education and Research (BMBF), PtJ-Bio, 0315883, the Leipzig Graduate School of Natural Sciences BuildMoNa of the German Science Foundation (DFG) and the German Leibniz Association (SAW-2011-IOM-2).

References

[1] Kokorin V V and Chernenko V A 1989 Martensitic transformation in ferromagnetic Heusler alloy *Fiz. Met. Metalloved.* **68** 1157–61
[2] Chernenko V A, Cesari E, Kokorin V V and Vitenko I N 1995 The development of new ferromagnetic shape memory alloys in Ni–Mn–Ga system *Scr. Metall. Mater.* **33** 1239–44
[3] Ullakko K 1996 Magnetically controlled shape memory alloys: a new class of actuator materials *J. Mater. Eng. Perform.* **5** 405–9
[4] Mahnke G, Seibt M and Mayr S G 2008 Microstructure and twinning in epitaxial NiMnGa films *Phys. Rev.* B **78**
[5] Eichhorn T, Hausmanns R and Jakob G 2011 Microstructure of freestanding single-crystalline Ni_2MnGa thin films *Acta Mater.* **59** 5067–73
[6] Edler T and Mayr S G 2010 Film lift-off from MgO: freestanding single crystalline Fe–Pd films suitable for magnetic shape memory actuation—and beyond *Adv. Mater.* **22** 4969–72
[7] O'Handley R C 1998 Model for strain and magnetization in magnetic shape-memory alloys *J. Appl. Phys.* **83** 3263
[8] Rabe U and Arnold W 1994 Acoustic microscopy by atomic force microscopy *Appl. Phys. Lett.* **64** 1493
[9] Yamanaka K, Ogiso H and Kolosov O 1994 Ultrasonic force microscopy for nanometer resolution subsurface imaging *Appl. Phys. Lett.* **64** 178
[10] Vree C 2009 Topographie, Struktur und Dynamik thermisch aufgedampfter Polymerfilme *PhD Thesis* Universität Göttingen http://webdoc.sub.gwdg.de/diss/2009/vree/
[11] Hohenberg P and Kohn W 1964 Inhomogeneous electron gas *Phys. Rev.* B **136** 864–71
[12] Vanderbilt D 1990 Soft self-consistent pseudopotentials in a generalized eigenvalue formalism *Phys. Rev.* B **41** 7892–5
[13] Rappe A, Rabe K, Kaxiras E and Joannopoulos J 1990 Optimized pseudopotentials *Phys. Rev.* B **41** 1227–30
[14] Kresse G and Hafner J 1994 Norm-conserving and ultrasoft pseudopotentials for first-row and transition elements *J. Phys.: Condens. Matter* **06** 8245–57
[15] Louie S, Froyen S and Cohen M 1982 Nonlinear ionic pseudopotentials in spin-density-functional calculations *Phys. Rev.* B **26** 1738–42
[16] Giannozzi P *et al* 2009 *J. Phys.: Condens. Matter* **21** 395502
[17] Perdew J P, Burke K and Ernzerhof M 1996 Generalized gradient approximation made simple *Phys. Rev. Lett.* **77** 3865–8
[18] Monkhorst H J and Pack J D 1976 Special points for Brillouin-zone integrations *Phys. Rev.* B **13** 5188–92
[19] Methfessel M and Paxton A 1989 High-precision sampling for Brillouin-zone integration in metals *Phys. Rev.* B **40** 3616–21

[20] Zayak A, Adeagbo W A, Entel P and Buchelnikov V D 2005 Crystal structures of Ni_2MnGa from density functional calculations *Phase Transit.* **78** 259–66
[21] Vlassak J J, Ciavarella M, Barber J R and Wang X 2003 The indentation modulus of elastically anisotropic materials for indenters of arbitrary shape *J. Mech. Phys. Solids* **51** 1701–21
[22] Gao Y F and Pharr G M 2007 Multidimensional contact moduli of elastically anisotropic solids *Scr. Mater.* **57** 13–6
[23] Rabe U 2006 Atomic force acoustic microscopy ed B Bhushan and H Fuchs *Applied Scanning Probe Methods II* (Berlin: Springer) pp 37–90
[24] Kopycinska-Müller M 2005 On the elastic properties of nanocrystalline materials and the determination of elastic properties on a nanoscale using the atomic force acoustic microscopy technique *PhD Thesis* Universität des Saarlandes, Saarbrücken
[25] Espinoza-Beltrán F J, Geng K, Muñoz Saldaña J, Rabe U, Hirsekorn S and Arnold W 2009 Simulation of vibrational resonances of stiff AFM cantilevers by finite element methods *New J. Phys.* **11** 083034
[26] Willis J R 1966 Hertzian contact of anisotropic bodies *J. Mech. Phys. Solids* **14** 163–76
[27] Vlassak J J and Nix W D 1993 Indentation modulus of elastically anisotropic half spaces *Phil. Mag.* A **67** 1045–56
[28] Jakob A M, Schmidt F, Müller M, Grundmann M, Höche T and Mayr S G 2012 in preparation
[29] Sader J E, Larson I, Mulvaney P and White L R 1995 Method for the calibration of atomic force microscope cantilevers *Rev. Sci. Instrum.* **66** 3789
[30] Hurley D C 2009 Contact resonance force microscopy techniques for nanomechanical measurements *Applied Scanning Probe Methods XI* ed B Bhushan and H Fuchs (Berlin: Springer) pp 97–138
[31] Ullakko K 1996 Magnetically controlled shape memory alloys: a new class of actuator materials *J. Mater. Eng. Perform.* **5** 405–9
[32] Martynov V V and Kokorin V V 1992 The crystal structure of thermally- and stress-induced martensites in Ni_2MnGa single crystals *J. Physique* III **2** 739–49
[33] Baron M P and Morin M 1997 Stress-induced transformation and temperature-induced transformation in Cu–Zn–Al single crystals *J. Physique* IV **07** C5-525-30
[34] Chernenko V A, L'vov V, Pons J and Cesari E 2003 Superelasticity in high-temperature Ni–Mn–Ga alloys *J. Appl. Phys.* **93** 2394
[35] Chernenko V A, Pons J, Cesari E and Ishikawa K 2005 Stress-temperature phase diagram of a ferromagnetic Ni–Mn–Ga shape memory alloy *Acta Mater.* **53** 5071–7
[36] Planes A, Mañosa L and Saxena A 2005 *Magnetism and Structure in Functional Materials (Springer Materials* vol 79*)* (Berlin: Springer)
[37] Johnson K L 1985 *Contact Mechanics* 1st edn (Cambridge: Cambridge University Press)
[38] Ozdemir Kart S and Cagın T 2010 Elastic properties of Ni_2MnGa from first-principles calculations *J. Alloys Compd.* **508** 177–83